communications materials

A Nature Portfolio journal

Article

https://doi.org/10.1038/s43246-025-01012-w

Elucidating and decoupling diverse fatigue mechanisms toward static self-recovery in ZrO_2-based antiferroelectrics

Haoji Qian[1], Rongzong Shen[2], Jiacheng Xu[2], Miaomiao Zhang[1], Minglei Ma[1], Yian Ding[1], Xiaoxi Li[1], Gaobo Lin[2], Jiani Gu[2], Ran Cheng[3], Yan Liu[1], Chengji Jin[1] ✉, Jiajia Chen[1] ✉, Yue Hao[1] & Genquan Han[1]

ZrO_2-based antiferroelectric (AFE) materials exhibit superior endurance compared to HfO_2-based ferroelectrics, making them promise for nanoelectronics. Nonetheless, their endurance properties remain insufficient for dynamic random-access memory applications. In this respect, the fundamental physical mechanisms underlying polarization fatigue and the intrinsic constraints on self-recovery remain poorly understood, yet they are pivotal for achieving fatigue-free operation. Here, we systematically decouple the multiple fatigue mechanisms in ZrO_2-based AFE capacitors and introduce a static self-recovery (SSR) method that significantly improves endurance. We present a three level traps model, developed by electrical measurements and first-principles calculations, that successfully describes the shallow/deep fatigue of ZrO_2-based AFE materials and their SSR processes. Moreover, the SSR effect can be significantly enhanced by optimizing the combination of break time and cycling unit. The proposed SSR methodology offers a viable solution to the endurance challenges of AFE random-access memory in practical applications, paving the way for high-endurance, energy-efficient memory technologies with enhanced functional versatility.

With the rapid advancement of artificial intelligence (AI) technologies, particularly deep learning models, traditional Si-based storage devices are facing growing challenges in terms of storage capacity, data transfer speeds, and energy efficiency[1–4]. In this context, non-volatile memory (NVM) devices emerge as a promising storage technology to overcome these issues. HfO_2-based ferroelectric (FE) materials have gained widespread attention for next-generation NVM applications, thanks to their exceptional compatibility with complementary metal-oxide-semiconductor (CMOS) technology[5–10]. Nonetheless, achieving dependable and stable electrical performance in HfO_2-based FE random-access memory (FeRAM) continues to be a significant challenge[11–14]. One of the key issues is the remnant polarization (P_r) degradation during electrical cycling, which is a concern regarding their reliability[15–21].

In comparison, ZrO_2-based antiferroelectric (AFE) devices exhibit more excellent endurance performance as reported[22–26]. Despite this, their endurance properties remain insufficient for dynamic random-access memory (DRAM)-level applications. The fundamental challenge lies in the limited understanding of the correlation between microscopic fatigue mechanisms and macroscopic electrical behavior in ZrO_2-based AFE devices, which hinders further advancements in their reliability and performance optimization. It has been revealed that the evolution of oxygen vacancies (V_O) plays a crucial role in the fatigue process of the metal-AFE-metal capacitor (Fig. 1a), which could be concluded as the coupling of V_O charge trapping, AFE to FE phase transition (PT) and V_O localization (Fig. 1b)[27]. A comprehensive understanding and decoupling of these three mechanisms will enable the development of a robust physical model, offering predictive and regulatory insights into the fatigue and recovery behaviors of ZrO_2-based AFE capacitors while potentially unveiling intriguing underlying physical phenomena (Fig. 1c).

In this article, by decoupling V_O charge trapping, a static self-recovery (SSR) method that does not require external circuitry is proposed, as well as the three level traps model, which could precisely describe the SSR process in ZrO_2-based capacitors. It is demonstrated that polarization fatigue can be effectively recovered by a certain break time (T_b), and shallow fatigue can be totally recovered (Fig. 1d), while deep fatigue cannot (Fig. 1e). Both the SSR behaviors under shallow and deep fatigue are successfully reproduced by the

[1]Hangzhou Institute of Technology and Faculty of Integrated Circuit, Xidian University, Xi'an, 710071, China. [2]Center of Computational Materials, Zhejiang Lab, Hangzhou, 311121, China. [3]College of Integrated Circuits, Zhejiang University, Hangzhou, 310058, China. ✉e-mail: cjjin@xidian.edu.cn; chenjiajia@xidian.edu.cn

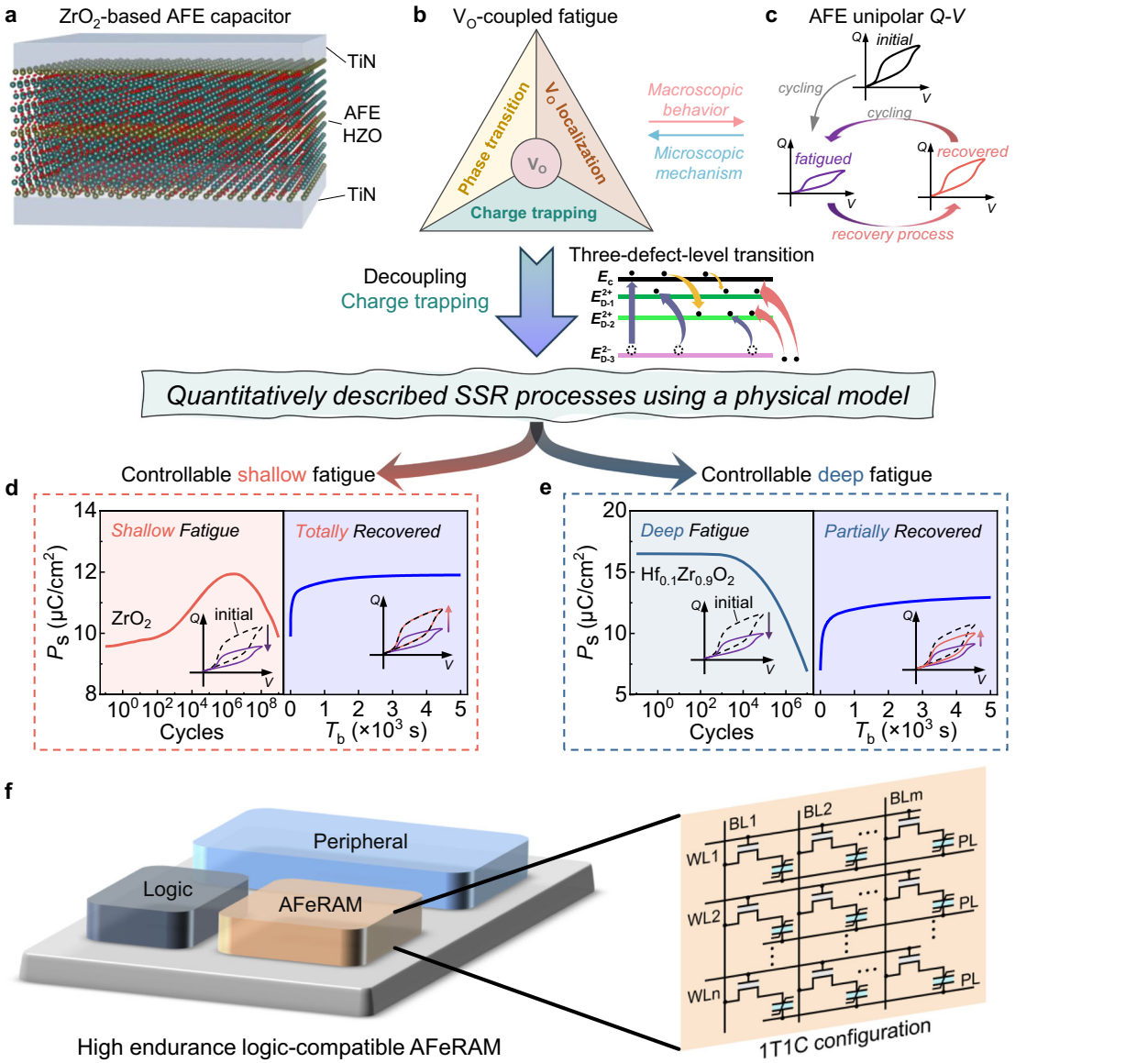

Fig. 1 | Proposal of the SSR method through elucidation of device fatigue mechanisms. a Schematic illustration of the AFE TiN/HZO/TiN capacitors. **b** V_O-coupled fatigue mechanisms in ZrO_2-based AFE capacitors. **c** Schematic diagram of the endurance enhancement in half-loop operated AFE devices via the recovery method. Development of predictable SSR method under (**d**) shallow and (**e**) deep fatigue situations in ZrO_2-based AFE capacitors by decoupling V_O charge trapping. Left panels are fatigue processes, and the right panels are recovery processes. The $Q-V$ curves of initial states are illustrated by black dashed lines. **f** Application of SSR method in high endurance logic-compatible AFeRAM utilizing half-loop operation with low operating voltage.

proposed three level traps model. Furthermore, by tuning the combination of T_b and the number of cycles for cycling unit, SSR ability for deep fatigue could be further optimized. This is due to the fast release of the shallow trapped charged V_O, which can effectively avoid deep fatigue. These controllable SSR processes hold promises for enhancing the endurance of logic-compatible AFE random-access memory (AFeRAM) (Fig. 1f).

Results and discussion

Electrical characteristics of ZrO_2-based AFE capacitors

AFE capacitors with the same top electrode (TE) and bottom electrode (BE) materials (Supplementary Fig. 1a) would show double hysteresis loop and zero spontaneous polarization. A lower operating voltage can be achieved by utilizing half-loop operation through build-in electric field modulation, as shown by schematic charge-voltage ($Q-V$) curves in Fig. 2a, primarily realized by engineering work function differences between TE and BE[24–26]. Therefore, investigating the electrical properties of half-loop is vital to the application of AFE capacitors. Figure 2b shows the measured polarization-voltage ($P-V$) curves of fabricated AFE $Hf_xZr_{1-x}O_2$ (HZO) capacitors by uni-directional positive-up-negative-down (uni-PUND) method, in which the positive (Pos.) and negative (Neg.) loops were recorded by applying +3.5 V and −3.5 V at 10 kHz, with the relax voltage (V_{relax}) maintained at +1.75 V and −1.75 V, respectively[28]. Here, $2P_{s,p}$ is used to quantitatively evaluate the AFE properties in actual applications with half-loop operation, as defined by the black arrow in the Pos. loop shown in Fig. 2b. The initial $2P_{s,p}$ value of ZrO_2 capacitor is 12.79 μC/cm², which is quite smaller than the one of $Hf_{0.1}Zr_{0.9}O_2$ capacitor (16.64 μC/cm²). Figure 2c shows the definition of full width at half maximum (*FWHM*) extracted from the current-voltage ($I-V$) curve, which is used to assess the spreading of coercive field (E_c) distribution. The *FWHM* of $I-V$ curve manifests the spatial dispersion of local E_c across the film. A small *FWHM* represents collective switching of all domains within a narrow electric field range, indicating a tightly distributed local E_c. Conversely, a large *FWHM* signifies asynchronous domain switching at varied electric fields, reflecting a dispersed local E_c distribution. The distribution of V_O would significantly modify the local E_c, substantially

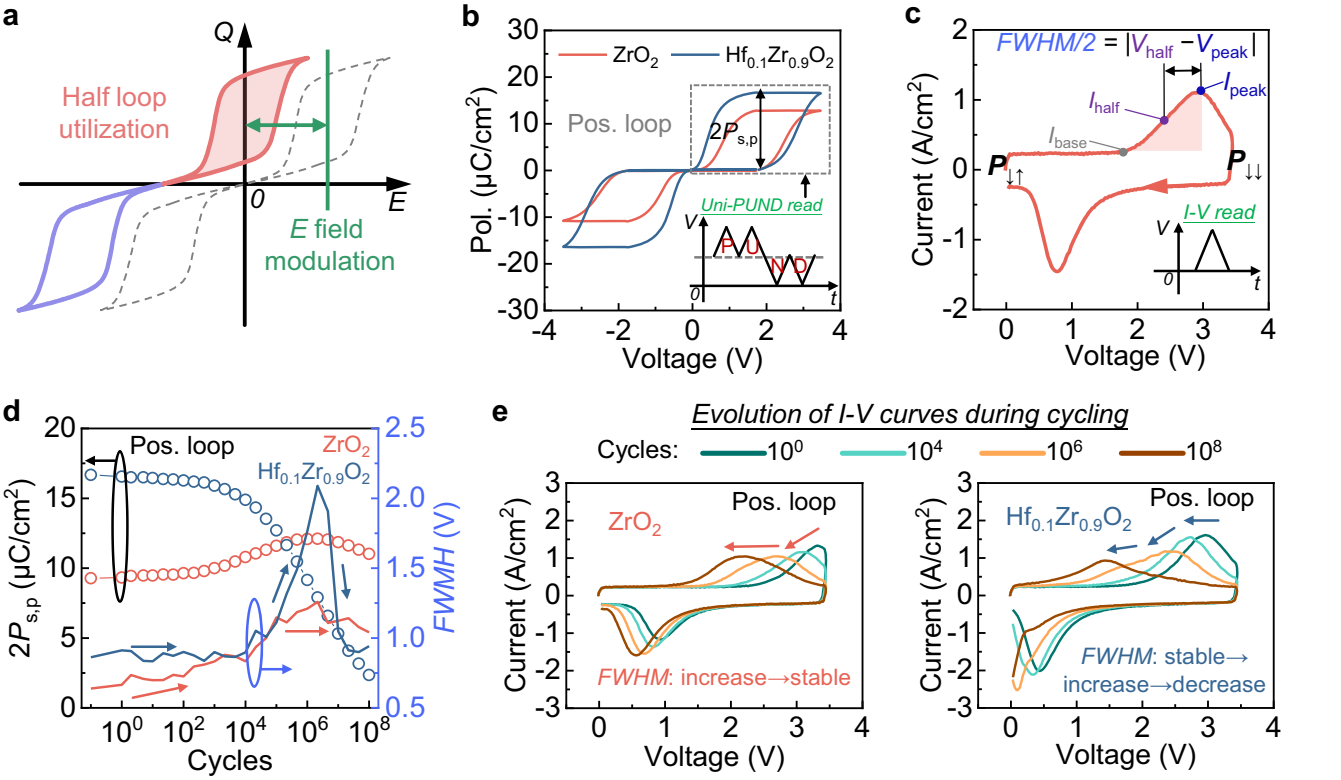

Fig. 2 | Electrical characteristics of ZrO_2 and $Hf_{0.1}Zr_{0.9}O_2$ capacitors. **a** Evolution of the $Q-V$ curve utilizing the half loop method for AFeRAM via electric field modulation. **b** Measured $P-V$ curve and $2P_{s,p}$ extracted from the Pos. loop, with the uni-PUND scheme shown in the inset. **c** $I-V$ curve of Pos. loop and the definition of *FWHM* for $P_{\uparrow\downarrow}$ to $P_{\downarrow\downarrow}$ switching current. **d** Evolution of $2P_{s,p}$ extracted from uni-PUND measurements, and *FWHM* derived from $I-V$ measurements for ZrO_2 and $Hf_{0.1}Zr_{0.9}O_2$ capacitors under +3.5 V, 200 kHz uni-directional cycling. **e** Evolution of $I-V$ curves for ZrO_2 and $Hf_{0.1}Zr_{0.9}O_2$ capacitors during uni-directional 10^8 cycles, with the trends of E_c and *FWHM* indicated by arrows and annotations. Changes in *FWHM* suggest the redistribution of V_O.

impacting polarization switching energy barriers. When V_O are uniformly distributed, the distribution of local E_c is tight and the *FWHM* is small. Oppositely, the inhomogeneous distributed V_O causes the broader distributed local E_c and a larger *FWHM*. A stable *FWHM* over cycling signifies the maintenance of stationary V_O distribution.

The comparison of $2P_{s,p}$ and *FWHM* evolutions between the ZrO_2 and $Hf_{0.1}Zr_{0.9}O_2$ capacitors during Pos. cycling with 3.5 V at 200 kHz is exhibited in Fig. 2d. The ZrO_2 capacitor shows wake-up effect with *FWHM* increasing until 2×10^6 cycles, then fatigue occurs with the stable *FWHM*. While the $Hf_{0.1}Zr_{0.9}O_2$ capacitor skips the wake-up process and begins fatigue after 5×10^3 cycles with *FWHM* first increasing and then decreasing. Figure 2e shows the evolution of $I-V$ curves with 10^8 cycles for the ZrO_2 and $Hf_{0.1}Zr_{0.9}O_2$ capacitors. Note that the changes in *FWHM*, including increase and decrease, indicate the redistribution of V_O[16,17]. During the cycling process, the stable *FWHM* with the shifted $I-V$ curve means that charge trapping occurs in the capacitor, without the redistribution of V_O, which may be the leading fatigue mechanism in ZrO_2 with 10^8 cycles. While the fatigue in $Hf_{0.1}Zr_{0.9}O_2$ may be induced by the coupling of V_O charge trapping and redistribution. The experimental measured electron energy loss spectroscopy (EELS) maps shown in Supplementary Fig. 2 provides direct evidence for the V_O redistribution by extracting the evolution of oxygen (O) K-edge doublet (*a*/*b* ratio) and supports the explanation of the *FWHM* broadening observed in the electrical measurements. The different fatigue behaviors observed between ZrO_2 and $Hf_{0.1}Zr_{0.9}O_2$ are strongly influenced by the presence of Hf. In pure ZrO_2, where no Hf is introduced, V_O tend to be charged during electrical cycling, characterized by the shift of $I-V$ curves with the limited change in the shapes of the curves. In contrast, in $Hf_{0.1}Zr_{0.9}O_2$, the introduction of Hf incorporation facilitates partial localization of V_O within the lattice and initiates AFE to FE PT, contributing to the significant change in the shapes of the $I-V$ curves.

Impact of fatigue mechanisms on the SSR characteristics

Endurance is a vital characteristic for memory devices. However, the endurance of AFE HZO devices reported so far is still insufficient to support DRAM-level applications. It has been extensively reported that recovery method is one of the most effective technologies to improve the endurance properties in FE and AFE materials. Figure 1c shows the schematic diagram of a typical recovery process. For HfO_2-based FE materials, higher electric field cycling is employed to recover the P_r fatigue caused by low electric field cycling, with its physical origin attributed to the redistribution of Vo[16]. The fatigue behaviors of HfO_2-based FE devices are fundamentally different with the ones of ZrO_2-based antiferroelectrics, where V_O charge trapping is not dominant. The ZrO_2-based AFE materials undergo a more complex phase transition process and fatigue mechanism, and the physical nature of its recovery has yet to be fully elucidated. In this article, guided by the exploration of the fatigue and recovery mechanisms, an SSR method is proposed for ZrO_2-based AFE capacitors. As shown in Supplementary Fig. 3b, the proposed SSR process can be briefly described as performing a certain period of break after cycling, realizing the self-recovery of polarization.

The comparison of SSR processes with 600 s break in ZrO_2 and $Hf_{0.1}Zr_{0.9}O_2$ capacitors is shown in Fig. 3a. The $2P_{s,p}$ of ZrO_2 capacitor decrease by 1.09 μC/cm² after 10^8 cycles and increase by 1.11 μC/cm² after 600 s break, which means complete recovery is realized within 600 s T_b. Here T_b is defined as the interval between the two continuous fatigue measurements for the same capacitor. Besides, Supplementary Fig. 4 and 5 show the evolutions of $2P_{s,p}$ and the corresponding *FWHM* during SSR processes with 0/600/1200 s T_b. For T_b = 600 s and 1200 s, $2P_{s,p}$ is totally recovered during break, and the *FWHM* during 2th to 5th fatigue measurements keeps stable, indicating that there is no V_O redistribution during

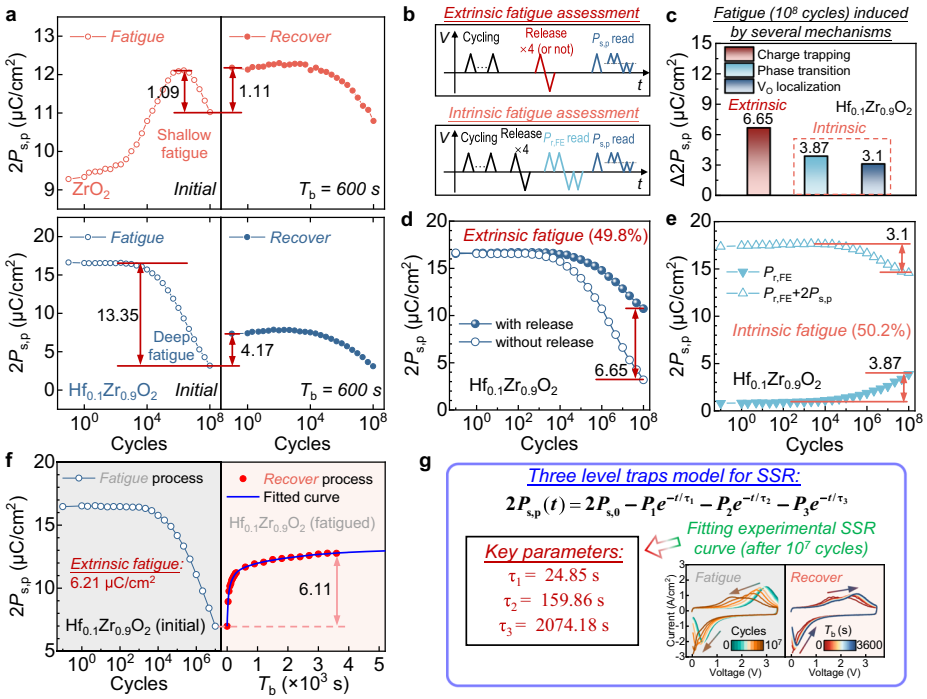

Fig. 3 | SSR characteristics and fatigue mechanisms analysis. a Comparison of SSR processes with T_b of 600 s for ZrO_2 and $Hf_{0.1}Zr_{0.9}O_2$ capacitors. **b** Voltage waveforms used for extrinsic and intrinsic fatigue assessments. **c** Summary of the contributions from various mechanisms to deep fatigue after 10^8 cycles for $Hf_{0.1}Zr_{0.9}O_2$. **d** Endurance characteristics of the $Hf_{0.1}Zr_{0.9}O_2$ capacitors, with and without charge release. **e** Evolution of $P_{r,FE}$ and $P_{r,FE} + 2P_{s,p}$ read by PUND and uni-PUND methods during 10^8 electrical cycling. **f** Fatigue and recover processes of $Hf_{0.1}Zr_{0.9}O_2$ capacitors under 10^7 cycles, with T_b of 3600 s. **g** Proposed three level traps model in this work, with insets showing the evolutions of $I-V$ curves during fatigue and SSR.

cycling. In this article, the totally recoverable fatigue in ZrO_2-based AFE capacitors under the SSR method is defined as shallow fatigue. In contrast, the $2P_{s,p}$ of $Hf_{0.1}Zr_{0.9}O_2$ capacitor exhibits a reduction of 13.35 μC/cm² after 10^8 cycles and increases by only 4.17 μC/cm² after 600 s break, corresponding to a recovery rate of 31.2%, and this partially recoverable fatigue in ZrO_2-based AFE capacitors under the SSR method is defined as deep fatigue.

It has been discussed in previous studies that there are three kinds of fatigue mechanisms in ZrO_2-based AFE capacitors, including V_O charge trapping, AFE to FE PT and V_O localization. The V_O charge trapping is classified as extrinsic fatigue, while the AFE to FE PT and V_O localization are classified as intrinsic fatigue[27]. As shown in Fig. 3a, the shallow fatigue in ZrO_2 capacitor may mainly originate from V_O charge trapping, thus is totally self-recoverable after a certain T_b. While the deep fatigue in $Hf_{0.1}Zr_{0.9}O_2$ may caused by the coupling of all these fatigue mechanisms. By using the assessing methods proposed in ref 27., the contributions of these three mechanisms to deep fatigue after 10^8 cycles $Hf_{0.1}Zr_{0.9}O_2$ capacitor are evaluated, and the voltage waveforms are shown in Fig. 3b. The fatigue values in $2P_{s,p}$ caused by these mechanisms are summarized in Fig. 3c, in which the extrinsic one (V_O charge trapping) is 6.65 μC/cm², accounting for 49.8% of the total $2P_{s,p}$ fatigue, and the detailed $2P_{s,p}$ versus cycles curves used to derive the assessed values are shown in Fig. 3d, e. It is evident that under 10^8 electrical cycles, the dominant fatigue mechanisms in ZrO_2 and $Hf_{0.1}Zr_{0.9}O_2$ capacitors diverge, leading to differences in their SSR behaviors. However, a comprehensive physical model capable of accurately describing and predicting the SSR characteristics of ZrO_2-based AFE capacitors remains elusive.

Development of three level traps model

After figuring out the proportional contributions of different mechanisms in deep fatigue situation of $Hf_{0.1}Zr_{0.9}O_2$, further analysis of the SSR capability at varying T_b is conducted, as illustrated by the red scatter plot in the right panel of Fig. 3f. The maximum self-recoverable polarization through SSR can be approximately estimated at 6.11 μC/cm² (the difference between the recovered $2P_{s,p}$ after SSR with a 3600 s break and the fatigued $2P_{s,p}$ after 10^7 cycles), nearly equivalent to the magnitude of extrinsic fatigue extracted from Fig. 3d, which is 6.21 μC/cm² for 10^7 cycles. This indicates that SSR can fully recover the extrinsic fatigue caused by charge trapping but has limited effectiveness in recovering intrinsic fatigue. Additional experiments on $Hf_{0.1}Zr_{0.9}O_2$ capacitors have been conducted to extend the endurance measurements to 10^9 cycles, and the ZrO_2 capacitors with inherently better endurance is expected to retain the $2P_{s,p}$ of ~7 μC/cm² even after 10^{12} cycles via proper SSR strategy (Supplementary Fig. 6). As shown in Supplementary Fig. 7, it is revealed that the recoverable $2P_{s,p}$ value (7.54 μC/cm²) shows excellent agreement with the measured extrinsic fatigue (7.22 μC/cm²), with a minor 4.4% difference. The alignment between these values at such high cycle counts provides compelling evidence that the break-time-dependent SSR process remains effective and that no significant new fatigue mechanisms emerge in this cycling regime. Notably, the totally self-recoverable shallow fatigue observed in ZrO_2 capacitors may also stem from V_O charge trapping. Due to the strong correlation between the SSR process and charge detrapping, the multi-level defect detrapping model is referenced in this article[29]. The charge decay in dielectrics follows multi-exponential kinetics due to traps with distinct energy depths, where detrapping rates depend on temperature and defect energy levels. A three level traps model is proposed, which successfully reproduces the evolution of $2P_{s,p}$ during SSR process in ZrO_2 and $Hf_{0.1}Zr_{0.9}O_2$ capacitors (Fig. 1d, e):

$$2P_{s,p}(t) = 2P_{s,0} - P_1 e^{-t/\tau_1} - P_2 e^{-t/\tau_2} - P_3 e^{-t/\tau_3} \quad (1)$$

where $P_{s,0}$, P_i and τ_i ($i = 1, 2, 3$) represent for the saturated polarization value after sufficiently long SSR, the self-recoverable polarization and the effective lifespan for the corresponding trap energy level, respectively.

As shown in Fig. 4a, the experimental SSR curves for $Hf_{0.1}Zr_{0.9}O_2$ after varying electrical cycles could also be fitted well. Besides, the shallow fatigue situation is also observed in $Hf_{0.1}Zr_{0.9}O_2$ capacitors, depending on the precisely controlled number of electrical cycles, highlighting the intrinsic unity of the SSR behaviors in both ZrO_2 and $Hf_{0.1}Zr_{0.9}O_2$ capacitors and the universality of the three level traps model. The relationship of self-recoverable polarization (P_i) and different electrical cycles could also be revealed, as illustrated by the orange scatter plot in Fig. 4b. These plots could

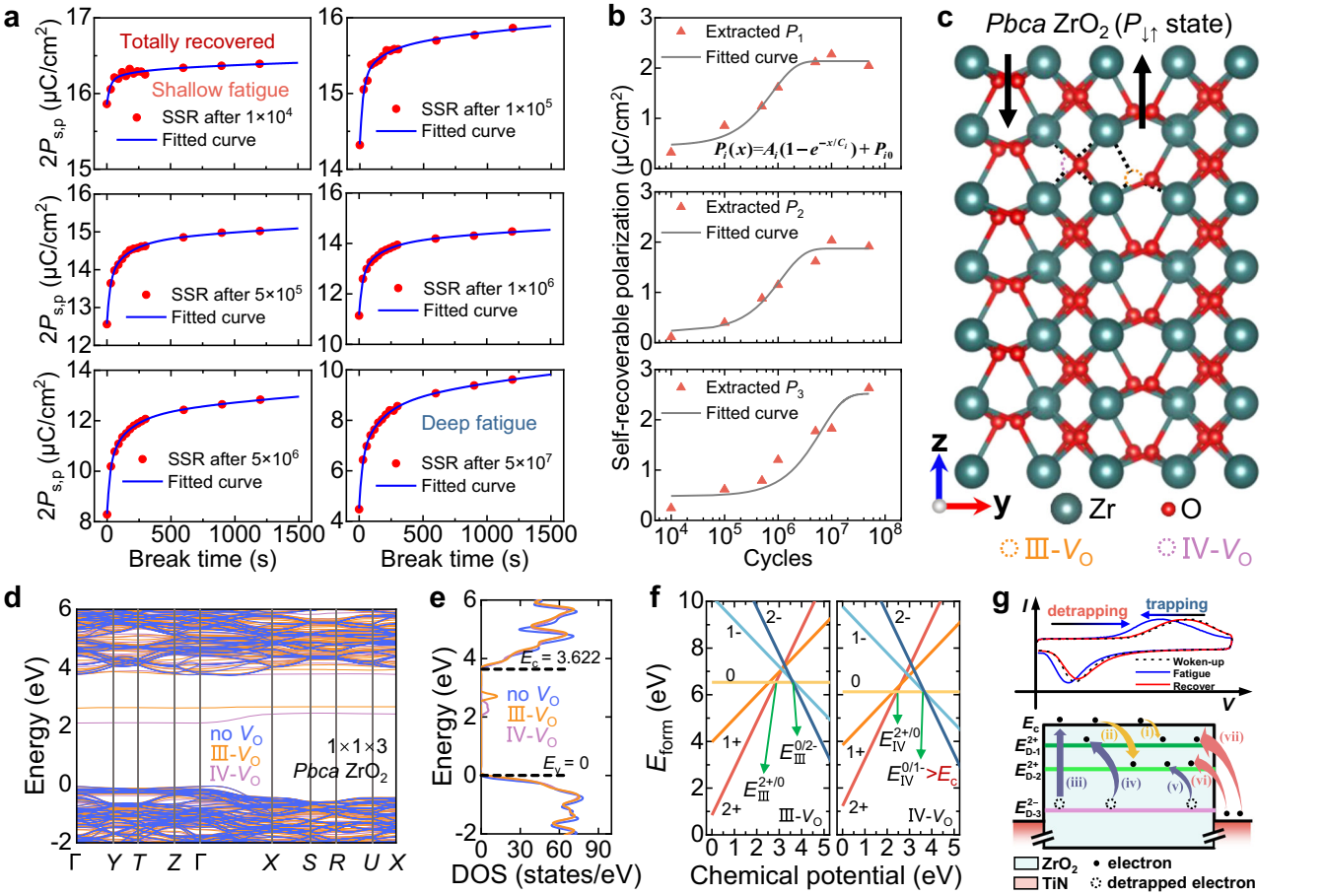

Fig. 4 | Theoretical demonstrations for three level traps model. a Experimental and fitted curves of the SSR processes in $Hf_{0.1}Zr_{0.9}O_2$ capacitors after different fatigue cycles, using the fixed τ parameters extracted from Fig. 3g. The specific fatigue cycles are 1×10^4, 1×10^5, 5×10^5, 1×10^6, 5×10^6 and 5×10^7, respectively. **b** Extracted values of P_1, P_2 and P_3 as a function of electrical cycles and their respective fitting curves. **c** Schematic diagram of $1 \times 1 \times 3$ *Pbca* ZrO_2 supercell, highlighting the locations of neutral III-V_O and IV-V_O, marked by orange and purple dashed circles, respectively. **d**, **e** First-principles calculated $E-k$ dispersion and DOS spectra for supercells with various O-deficient configurations. **f** Plot of the formation energy of different charged V_O as a function of the chemical potential. **g** Schematic illustration of mechanism for SSR and possible detrapping routes for E_{D-1}^{2+}: (i), (iv), (vii); E_{D-2}^{2+}: (ii), (v), (vi); E_{D-3}^{2-}: (iii), (iv), (v).

be described as (gray curves in Fig. 4b):

$$P_i(x) = A_i(1 - e^{-x/C_i}) + P_{i0} \quad (2)$$

where C_i is the numbers of electrical cycles that saturate P_i, P_{i0} is the initial trapped charge.

Furthermore, the three level traps model can be supported by density functional theory (DFT) calculations. Here, $1 \times 1 \times 3$ *Pbca* ZrO_2 supercells are constructed to theoretically calculate the trap energy level distributions, as shown in Fig. 4c. The O-deficient configurations are constructed by removing one O atom from the supercells, with the orange and purple dashed circles marking the localizations of neutral III-V_O and IV-V_O, respectively. Considering the primary aim of evaluating the electronic structure of AFE ZrO_2 in its antipolar ground state, the two selected V_O positions (one III-O site and one IV-O site) are sufficient to capture the representative variation in local environments and corresponding defect level distributions, owing to the presence of inversion symmetry. Then, the bulk electronic band structure calculations of supercells with different O-deficient configurations were performed. Figure 4d, e plot the calculated energy-momentum ($E-k$) dispersion and density of states (DOS) of ZrO_2 supercells with neutral III-V_O, IV-V_O and without V_O. The band gap between valance band maximum and conduction band minimum is around 3.622 eV, and the localizations of defect energy levels for neutral III-V_O and IV-V_O are confirmed. The formation energies for V_O could be theoretically estimated by:

$$E_q^{form}(\mu_e) = E_q^{N-1} + \frac{1}{2}E(O_2) + q\mu_e - E^N \quad (3)$$

where E_q^{N-1} is the total energy of the supercell with different charged Vo, N is the number of total atoms, q is the charge number, $E(O_2)$ is the energy of an isolated oxygen molecule, μ_e is the chemical potential, and E^N is the total energy of the supercell without V_O.

The calculated formation energies of the different charged V_O as a function of μ_e are illustrated in Fig. 4f, and three transition levels are confirmed as $E_{III}^{2+/0}$, $E_{III}^{0/2-}$ and $E_{IV}^{2+/0}$, indicating V_O are more likely to be charged at three trap energy levels during cycling, which are named as E_{D-1}^{2+}, E_{D-2}^{2+} and E_{D-3}^{2-}. Assuming that these three trap energy levels are all above the middle of band gap, and their relative positions are schematically illustrated in Fig. 4g. Possible V_O detrapping routes for E_{D-1}^{2+} are: (i) electrons transition from conduction band (E_c), (iv) electrons transition from E_{D-3}^{2-} to E_{D-1}^{2+}, (vii) tunneling electrons from electrodes; for E_{D-2}^{2+} are: (ii) electrons transition from E_c, (v) electrons transition from E_{D-3}^{2-} to E_{D-2}^{2+}, (vi) tunneling electrons from electrodes; for E_{D-3}^{2-} are: (iii) electrons transition from E_{D-3}^{2-} to E_c, (iv) electrons transition from E_{D-3}^{2-} to E_{D-1}^{2+}, (v) electrons transition from E_{D-3}^{2-} to E_{D-2}^{2+}. The energy level differences associated with electron detrapping from V_O during the self-recovery of extrinsic fatigue are

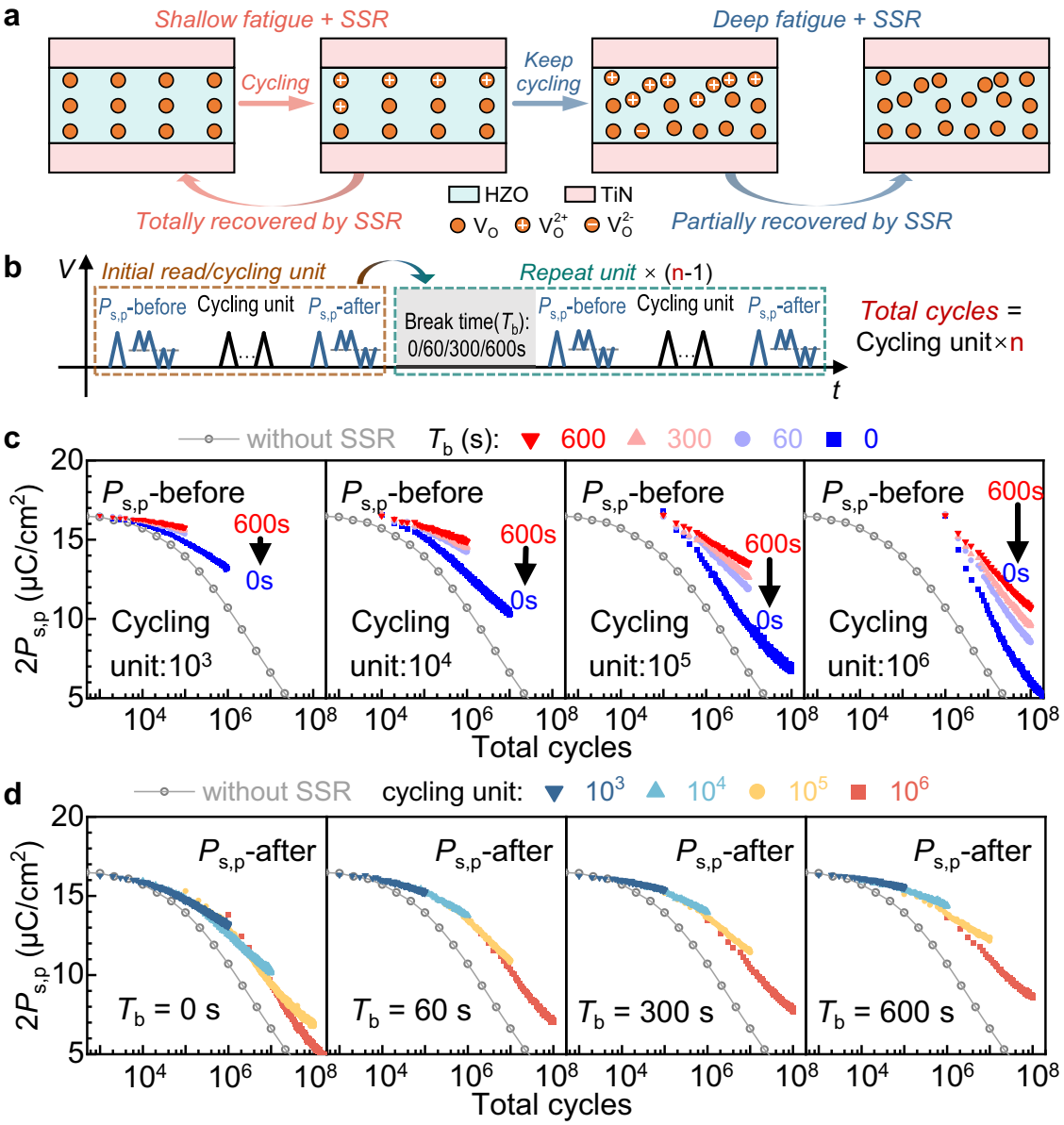

Fig. 5 | Application of SSR in $Hf_{0.1}Zr_{0.9}O_2$ capacitors during continuous cycling processes. a Schematic diagrams of V_O evolutions during shallow/deep fatigue and corresponding SSR processes. **b** Voltage waveform for continuous cycling unit and the timing of $P_{s,p}$-before and $P_{s,p}$-after read. **c** Comparison of $P_{s,p}$-before and **d** $P_{s,p}$-after under different T_b and cycling unit. Both of increasing T_b and decreasing cycling unit can improve endurance.

indeed thermally surmountable through two key mechanisms: (1) The effective detrapping rate from deep traps (~1.0-1.2 eV) follows a Boltzmann distribution where a small but non-zero fraction of carriers ($\exp(-E_a/k_BT)$) can overcome the barrier at room temperature, especially given the high attempt frequency (~10^{12} s^{-1}) in oxide materials, (2) the observed recovery of deep fatigue occurs over macroscopic timescales (10^2-10^3 s), allowing sufficient time for statistically rare thermal excitation events to accumulate. This is evidenced by our three-level trap model's excellent fit to the recovery kinetics (with τ_1 ~ 24.85 s, τ_2 ~ 159.86 s, τ_3 ~ 2074.18 s) inherently accounts for thermally activated detrapping processes.

Optimization of cycling unit and T_b combination

It has been proved above that the shallow fatigue can be totally recovered by SSR, and for deep fatigue, the extrinsic P_r degradation caused by charge trapping can also be totally recovered by SSR, while the intrinsic one cannot. Figure 5a presents the schematic diagrams illustrating V_O evolutions during both shallow and deep fatigue conditions, as well as the corresponding SSR processes. These visualizations clearly elucidate the mechanisms that lead to both totally and partially recovered polarization degradation.

It is worth considering how to effectively apply SSR to further improve the endurance of devices. Therefore, the abilities of SSR with various combinations of different cycling unit and T_b in $Hf_{0.1}Zr_{0.9}O_2$ capacitors are investigated, in which the cycling unit is defined as several continuous electrical cycles. Figure 5b shows the measurement scheme, in which the repeat unit is defined as the combination of T_b, read before cycling ($P_{s,p}$-before), cycling unit and read after cycling ($P_{s,p}$-after). Different degrees of endurance improvement are realized by applying various combinations of cycling unit (10^3/10^4/10^5/10^6 cycles) and T_b (0/60/300/600 s), and the fatigue without SSR is also plotted as a reference. Figure 5c, d show the comparison of $P_{s,p}$-before and $P_{s,p}$-after under different T_b and cycling unit. For fixed cycling unit, the SSR effect is greatly enhanced with increasing T_b, shown in Fig. 5c. This means that during the cycling, the more charges trapped in the ZrO_2-based AFE devices are released by SSR, thus preventing deep fatigue, the more effective endurance can be enhanced. And for fixed T_b, the

endurance can be improved with decreasing cycling unit, shown in Fig. 5d. This means that during a single cycling unit, a lower accumulation of trapped charges may enhance the efficacy of SSR in enhancing endurance. Notably, while employing Keysight B1530A Waveform Generator to perform these electrical measurements, a brief delay is inherently introduced by the measurement system itself. Specifically, during the automatic switching between the cycling and readout modules within the test sequence, a finite recovery time approximately 0.8 seconds is inevitably incurred. This delay, although not user-defined, can provide partial recovery for the device, thereby contributing to the observed endurance improvement even under nominal $T_b = 0$ s conditions. Finally, it has been demonstrated that avoiding deep charge trapping by SSR is effective for the endurance improvement of the ZrO_2-based AFE devices. To further support this approach, a self-sensing circuit has been proposed (Supplementary Fig. 8), which could potentially enable SSR application in future implementations.

Conclusions

In summary, through an in-depth investigation of the fatigue behavior in AFE ZrO_2 and $Hf_{0.1}Zr_{0.9}O_2$ capacitors, we successfully decouple the contribution of V_O charge trapping and uncover the underlying SSR phenomenon. A three level traps model is proposed, which can reproduce and predict the evolution of $2P_{s,p}$ during SSR process. The proposed mechanisms for SSR are confirmed by DFT calculations and summarized in Fig. 4. Then, the ability of SSR for deep fatigue was investigated. The introducing of SSR in the break of two cycling processes could effectively relieve fatigue. By optimizing the combination of T_b and cycling unit to avoid deep fatigue (decrease the concentration of deep trapped charged V_O), the endurance performance would be greatly improved. The utilization of SSR shows promise in addressing the endurance issues of AFeRAM in practical applications.

Methods

Device fabrication

The fabrication of $ZrO_2/Hf_{0.1}Zr_{0.9}O_2$ AFE capacitors starts from silicon (Si) substrate. After conventional RCA wet clean, a 50 nm-thick TiN layer is deposited as bottom electrode (BE) on Si substrate by reactive sputtering. Then, the samples are loaded into the atomic layer deposition (ALD) chamber for 10 min O_3 treatment on TiN BE[23]. Next, 10 nm $ZrO_2/Hf_{0.1}Zr_{0.9}O_2$ AFE film is in situ deposited via ALD using tetrakis-dimethylamino hafnium (TDMAHf) and tetrakis-dimethylamino zirconium (TDMAZr) as precursors, and H_2O as oxidant at 250 °C. The growth rates of HfO_2 and ZrO_2 are 0.71 and 0.67 Å/cycle, respectively. During the deposition of $Hf_{0.1}Zr_{0.9}O_2$ AFE film, HfO_2 cycles are uniformly inserted in ZrO_2 cycles, and one HfO_2 cycle followed by nine ZrO_2 cycles as a supercycle is employed. Subsequently, 50 nm-thick TiN is deposited by reactive sputtering and patterned for top electrode (TE). The size of characterized devices is 11304 μm^2. Finally, post-metallization annealing (PMA) at 500 °C for 30 s in N_2 atmosphere is performed to crystallize $ZrO_2/Hf_{0.1}Zr_{0.9}O_2$ films.

Characterizations

Cross-sectional transmission electron microscope (TEM) measurements were performed on a Thermofisher Talos F200X to confirm the metal-AFE-metal structure of fabricated AFE HZO capacitors and the thickness for HZO film. GIXRD measurements were carried out on a Bruker D8 Discover (Cu-Kα radiation, $\lambda = 0.154$ nm) for structural analysis of the capacitors. Electrical measurements were carried out on aixACCT TF Analyzer 3000 and Keysight B1500A semiconductor device analyzer.

First-principles calculations

Band structures were calculated in the framework of DFT using the QUANTUM ESPRESSO v6.8 package. Ultrasoft pseudopotentials with generalized gradient approximation (GGA) and Perdew-Burke-Ernzerhof (PBE) exchange correlation were used[30–32]. The 1 × 1 × 3 supercells with different O-deficient configurations were constructed based on the ZrO_2 primitive cell with *Pbca* space group (a = 5.126 Å, b = 10.037 Å, and c = 5.102 Å). According to the convergence tests, the kinetic energy cutoff for the electron wavefunctions is set as 816 eV, and an 8 × 4 × 3 Monkhorst-Pack k-point sampling is used for the Brillouin zone integration in the structure relaxation.

Data availability

The source data of all the plots of main manuscript and Supplementary Information are available as Supplementary Data.

Received: 1 April 2025; Accepted: 6 November 2025;
Published online: 20 November 2025

References

1. Merolla, P. A. et al. A million spiking-neuron integrated circuit with a scalable communication network and interface. *Science* **345**, 668–673 (2014).
2. Silver, D. et al. Mastering the game of Go with deep neural networks and tree search. *Nature* **529**, 484–489 (2016).
3. Zhang, W. et al. Neuro-inspired computing chips. *Nat. Electron* **3**, 371–382 (2020).
4. Zhu, J., Zhang, T., Yang, Y. & Huang, R. A comprehensive review on emerging artificial neuromorphic devices. *Appl. Phys. Rev.* **7**, 011312 (2020).
5. Böscke, T. S., Müller, J., Bräuhaus, D., Schröder, U. & Böttger, U. Ferroelectricity in hafnium oxide thin films. *Appl. Phys. Lett.* **99**, 102903 (2011).
6. Müller, J. et al. Ferroelectricity in yttrium-doped hafnium oxide. *J. Appl. Phys.* **110**, 114113 (2011).
7. Park, M. H. et al. Ferroelectricity and Antiferroelectricity of Doped Thin HfO_2-Based Films. *Adv. Mater.* **27**, 1811–1831 (2015).
8. Mikolajick, T. et al. Next Generation Ferroelectric Memories enabled by Hafnium Oxide. in *2019 IEEE International Electron Devices Meeting (IEDM)* 15.5.1-15.5.4 (IEEE, San Francisco, CA, USA, 2019).
9. Hoffmann, M. et al. Intrinsic Nature of Negative Capacitance in Multidomain $Hf_{0.5}Zr_{0.5}O_2$-Based Ferroelectric/Dielectric Heterostructures. *Adv. Funct. Mater.* **32**, 2108494 (2022).
10. Jan, A. et al. In Operando Optical Tracking of Oxygen Vacancy Migration and Phase Change in few Nanometers Ferroelectric HZO Memories. *Adv. Funct. Mater.* **33**, 2214970 (2023).
11. Rushchanskii, K. Z., Blügel, S. & Ležaić, M. Ordering of Oxygen Vacancies and Related Ferroelectric Properties in $HfO_{2-\delta}$. *Phys. Rev. Lett.* **127**, 087602 (2021).
12. Mikolajick, T., Slesazeck, S., Park, M. H. & Schroeder, U. Ferroelectric hafnium oxide for ferroelectric random-access memories and ferroelectric field-effect transistors. *MRS Bull.* **43**, 340–346 (2018).
13. Park, M. H., Lee, Y. H., Mikolajick, T., Schroeder, U. & Hwang, C. S. Review and perspective on ferroelectric HfO_2-based thin films for memory applications. *MRS Commun.* **8**, 795–808 (2018).
14. Lin, Y.-J. et al. Role of electrode-induced oxygen vacancies in regulating polarization wake-up in ferroelectric capacitors. *Appl. Surf. Sci.* **528**, 147014 (2020).
15. Gong, Z. et al. Physical origin of the endurance improvement for HfO_2-ZrO_2 superlattice ferroelectric film. *Appl. Phys. Lett.* **121**, 242901 (2022).
16. Chen, J. et al. Physical Origin of Recovable Ferroelectric Fatigue and Recovery for Doped-HfO_2: Toward Endurance Immunity. in *2023 International Electron Devices Meeting (IEDM)* 18.1.1-18.1.4 (IEEE, San Francisco, CA, USA, 2023).
17. Chen, J. et al. Impact of Oxygen Vacancy on Ferroelectric Characteristics and Its Implication for Wake-Up and Fatigue of HfO_2-Based Thin Films. *IEEE Trans. Electron Devices* **69**, 5297–5301 (2022).
18. Cheng, Y. et al. Reversible transition between the polar and antipolar phases and its implications for wake-up and fatigue in HfO_2-based ferroelectric thin film. *Nat. Commun.* **13**, 645 (2022).

19. Gong, T. et al. 10^5× Endurance Improvement of FE-HZO by an Innovative Rejuvenation Method for 1z Node NV-DRAM Applications. in *2021 IEEE Symposium on VLSI Technology (VISI)* 1-2 (IEEE, Kyoto, Japan, 2021).
20. Liao, P. J. et al. Characterization of Fatigue and Its Recovery Behavior in Ferroelectric HfZrO. in *2021 IEEE Symposium on VLSI Technology (VISI)* 1-2 (IEEE, Kyoto, Japan, 2021).
21. Liu, Z. et al. Reversible fatigue-rejuvenation procedure and its mechanism in $Hf_{0.5}Zr_{0.5}O_2$ epitaxial films. *J. Phys.: Condens. Matter* **35**, 204002 (2023).
22. Hsiang, K.-Y. et al. Novel Opposite Polarity Cycling Recovery (OPCR) of $HfZrO_2$ Antiferroelectric-RAM with an Access Scheme Toward Unlimited Endurance. in *2022 International Electron Devices Meeting (IEDM)* 32.5.1-32.54 (IEEE, San Francisco, CA, USA, (2022).
23. Qian, H. et al. Boost Antiferroelectricity in ZrO_2-Based Capacitors by Ozone Treatment on Bottom Electrode. *IEEE Trans. Electron Devices* **71**, 8016–8020 (2024).
24. Pesic, M., Schroeder, U., Slesazeck, S. & Mikolajick, T. Comparative Study of Reliability of Ferroelectric and Anti-Ferroelectric Memories. *IEEE Trans. Device Mater. Relib.* **18**, 154–162 (2018).
25. Pesic, M. et al. Anti-ferroelectric-like ZrO_2 non-volatile memory: Inducing non-volatility within state-of-the-art DRAM. in *2017 17th Non-Volatile Memory Technology Symposium (NVMTS)* 1-4 (IEEE, Aachen, 2017).
26. Xu, J. et al. Anti-Ferroelectric ZrO_2 Capacitors With Ultralow Operating Voltage (<1.2 V) and Improved Endurance Toward Logic Compatible eDRAM. *IEEE Trans. Electron Devices* **71**, 5767–5770 (2024).
27. Qian, H. et al. Dynamic evolution of oxygen vacancies during cycling in antiferroelectric $Hf_xZr_{1-x}O_2$. *Appl. Phys. Lett.* **124**, 243508 (2024).
28. Magagnin, G. et al. An Original Positive-Up-Negative-Down Protocol for Electrical Characterization of Antiferroelectric Materials. *Nano Lett.* **25**, 6686–6692 (2025).
29. Chen, G. & Xu, Z. Charge trapping and detrapping in polymeric materials. *J. Appl. Phys.* **106**, 123707 (2009).
30. Kresse, G. & Hafner, J. Ab initio molecular dynamics for liquid metals. *Phys. Rev. B* **47**, 558 (1993).
31. Kresse, G. & Furthmüller, J. Efficient iterative schemes for ab initio total-energy calculations using a plane-wave basis set. *Phys. Rev. B* **54**, 11169 (1996).
32. Kresse, G. & Joubert, D. From ultrasoft pseudopotentials to the projector augmented-wave method. *Phys. Rev. B* **59**, 1758 (1999).

Acknowledgements

This work was supported in part by the National Natural Science Foundation of China under Grant 62204229, Grant 62204228; in part by the Zhejiang Provincial Natural Science Foundation (No. LQ24A040010).

Author contributions

H.Q., C.J. and J.C. proposed and implemented the project. R.S., J.X., M.Z., M.M., Y.D. X.L. G.L. J.G. and R.C. fabricated the devices and performed the experimental verification of the device structures. H.Q. conducted electrical measurements and first-principles calculations. Y.L., Y.H. and G.H. helped with data analysis. All authors contributed to write up of the manuscript. G.H. organized and supervised the whole project implementation and provided the project financial support.

Competing interests

The authors declare no competing interests.

Additional information

Supplementary information The online version contains supplementary material available at https://doi.org/10.1038/s43246-025-01012-w.

Correspondence and requests for materials should be addressed to Chengji Jin or Jiajia Chen.

Peer review information *Communications Materials* thanks the anonymous reviewers for their contribution to the peer review of this work. A peer review file is available.